

LA-UR-17-25300

Approved for public release; distribution is unlimited.

Title: Failure Diameter of PBX 9502: Simulations with the SURFplus model

Author(s): Menikoff, Ralph

Intended for: Report

Issued: 2017-07-03

Disclaimer:

Los Alamos National Laboratory, an affirmative action/equal opportunity employer, is operated by the Los Alamos National Security, LLC for the National Nuclear Security Administration of the U.S. Department of Energy under contract DE-AC52-06NA25396. By approving this article, the publisher recognizes that the U.S. Government retains nonexclusive, royalty-free license to publish or reproduce the published form of this contribution, or to allow others to do so, for U.S. Government purposes. Los Alamos National Laboratory requests that the publisher identify this article as work performed under the auspices of the U.S. Department of Energy. Los Alamos National Laboratory strongly supports academic freedom and a researcher's right to publish; as an institution, however, the Laboratory does not endorse the viewpoint of a publication or guarantee its technical correctness.

FAILURE DIAMETER OF PBX 9502: SIMULATIONS WITH SURFPLUS MODEL

RALPH MENIKOFF

June 28, 2017

Abstract

SURFplus is a reactive burn model for high explosives aimed at modelling shock initiation and propagation of detonation waves. It utilizes the SURF model for the fast hot-spot reaction plus a slow reaction for the energy released by carbon clustering. A feature of the SURF model is that there is a partially decoupling between burn rate parameters and detonation wave properties. Previously, parameters for PBX 9502 that control shock initiation had been calibrated to Pop plot data (distance-of-run to detonation as a function of shock pressure initiating the detonation). Here burn rate parameters for the high pressure regime are adjusted to fit the failure diameter and the limiting detonation speed just above the failure diameter. Simulated results are shown for an unconfined rate stick when the 9502 diameter is slightly above and slightly below the failure diameter. Just above the failure diameter, in the rest frame of the detonation wave, the front is sonic at the PBX/air interface. As a consequence, the lead shock in the neighborhood of the interface is supported by the detonation pressure in the interior of the explosive rather than the reaction immediately behind the front. In the interior, the sonic point occurs near the end of the fast hot-spot reaction. Consequently, the slow carbon clustering reaction can not affect the failure diameter. Below the failure diameter, the radial extent of the detonation front decreases starting from the PBX/air interface. That is, the failure starts at the PBX boundary and propagates inward to the axis of the rate stick.

1 Introduction

High explosive (HE) reactive burn models are used in simulations for initiation and propagation of detonation waves. Typically, burn models are physically motivated but have parameters that need to be calibrated to experimental data. Here we focus on the SURFplus model [[Menikoff and Shaw, 2010, 2012](#)]. The model has fast and slow burn rates associated with hot spot burning (SURF model) and the energy release from carbon clustering, respectively.

A feature of SURFplus is that the burn rate as a function of the lead shock pressure is defined piecewise on pressure intervals. Each pressure interval dominates a different detonation wave phenomenon; low pressure shock initiation regime, intermediate pressure failure diameter, corner turning and dead zone regime, high pressure regime for the curvature effect of propagating detonation waves. This leads to a partially decoupling between burn rate parameters and detonation wave properties, which facilitates calibrating model parameters.

In a previous report [[Menikoff, 2017a](#)], we discussed a strategy for calibrating the SURF model and then used it to fit parameters for shock initiation of PBX 9502; burn rate up to shock pressure of about 18 GPa. Here we extend the 9502 calibration to higher shock pressures by fitting to failure diameter data of [Campbell \[1984\]](#).

The failure diameter is the smallest diameter of an unconfined rate stick for which a steady detonation wave will propagate. It is sensitive to the burn rate for the pressure interval between the sonic point on the reactants shock polar and the CJ pressure. We note for PBX 9502 that the sonic pressure is near the high end of shock pressure on the measured Pop plot (distance-of-run to detonation for initiation by a sustained shock). In addition, failure diameter experiments measure the limiting detonation speed just above the failure diameter. The limiting detonation speed depends on the curvature of the detonation front on axis and the curvature effect, detonation speed as a function of local front curvature; see for example, [[Bdzil and Stewart, 2007](#)]. The curvature effect is largely determined by the reaction-zone width of a propagating detonation wave. The reaction-zone width is largely determined by the burn rate at high shock pressures; interval between the CJ pressure and VN spike pressure.

The PBX 9502 EOS, SURF burn rate and the parameters that control the failure diameter and the limiting detonation speed are discussed in section 2. Also discussed is the issue that experimental data show the curvature effect for PBX 9502 varies with lot [see [Hill and Aslam, 2010, fig. 6](#)]. Very likely variations of grain scale heterogeneities affect the burn rate and hence the reaction-zone width which dominates the curvature effect.

For rate parameters which best fit the failure diameter data, the results of rate stick simulations for PBX 9502 with diameters slightly above and slightly below the failure diameter are

shown in section 3. With the rate stick diameter slightly above the failure diameter, the simulation shows that the lead shock is near sonic at the HE interface with a pressure of about 15 GPa. The sonic state at the interface is in agreement with the analysis of [Trofimov and Dremin, 1971, see fig. 1c], [Bdzil, 1981, see fig. 14] and numerical simulations [Gamezo and Oran, 1997, see fig. 1].

The sonic boundary condition implies that the lead shock in the neighborhood of the interface is supported by the detonation pressure at smaller radii rather than the reaction immediately behind the front. This is important since the boundary condition strongly influences the shape of the detonation front and hence the detonation speed. It also sets the low end of the pressure interval for the burn rate that determines the failure diameter.

Moreover, in the interior of the rate stick, the sonic point is near the end of the fast reaction. This implies that the failure diameter is determined by the fast rate; *i.e.*, the energy released from the slow rate occurs too far behind the front to affect whether or not failure occurs.

For a rate stick diameter slightly below the failure diameter, the simulation started with a detonation wave in the PBX 9502. The simulation shows that the lead shock pressure decreases smoothly until the detonation wave fails. The pressure decrease starts at the PBX interface and propagates inward. That is, as expected, the failure begins at the boundary of the HE and progresses to the interior.

Results and implication of fitting the rate to the failure diameter and simulations above and below the failure diameter are summarized in section 4.

2 EOS & Burn rate

Before discussing the extension of the burn rate calibration to the failure diameter, we review the PBX 9502 equation of state used in the previous calibration of the SURFplus model to shock initiation data [Menikoff, 2017a].

The failure diameter is determined as the limiting case of experiments measuring the diameter effect (detonation speed as a function of diameter for an unconfined rate stick [Campbell, 1984]); *i.e.*, the failure diameter is the smallest diameter for which a steady detonation wave can propagate. The other limiting case, extrapolating the detonation speed to infinite diameter, determines the planar or CJ detonation speed.

While the failure diameter for a PBX does depend on the HE lot due to variation of the hot-spot burn rate with grain scale heterogeneities, the CJ detonation speed should depend only on the equation of state of the HE products and the initial state (ρ_0, e_0) of the reactants. Assuming the mass fraction of binder is well controlled, the products EOS should be independent of lot.

For the diameter effect data of [Campbell \[1984\]](#), extrapolating the detonation speed linearly in $1/\text{radius}$ for the 2 two largest diameter rate sticks gives a CJ detonation speed of 7.782 km/s. This is a little over 1 % higher than the CJ detonation speed (7.700 km/s) of the products EOS previously used. We note that the smaller detonation speed results from extrapolating earlier diameter effect data of [Campbell and Engelke \[1976\]](#), see fig. 5a for X-0290 (developmental version of 9502)]. The difference in extrapolation is due to the non-linearity of the detonation speed as a function of $1/\text{radius}$ at large radii, as seen in [[Campbell, 1984](#), fig. 3], and the range of the earlier data up to a 1 inch rate stick while the later experiments extended the data up to a 4 inch rate stick.

The EOS can be fine tuned to correct the detonation speed with minimal effect on the CJ release isentrope by a combination of an energy shift and a linear scaling of the specific volume as shown in [[Menikoff, 2017b](#)]. The corrected products EOS is used for the simulations discussed in this report. The CJ state for the corrected EOS is listed in [table 1](#). Also shown is the lower CJ state without the energy release from the second slow (carbon clustering) reaction. Part of the curvature effect for moderate to large curvature ($\kappa > 0.1 \text{ mm}^{-1}$) results from the sonic point shifting to the end of the fast reaction and having less reaction energy to support the detonation. The remainder of the curvature effect is due to the reaction-zone width.

The shift in the sonic point gives rise to the non-linearity in the detonation speed for large diameter rate sticks that affects the extrapolation of diameter effect data to the infinite diameter CJ detonation speed. This is also why we use the SURFplus model rather than the SURF model for PBX 9502.

Table 1: CJ detonation state for PBX 9502 based on corrected model EOS.

	V cm $^3/\text{g}$	e MJ/kg	P GPa	T K	u_p km/s	c km/s
Init state	0.52798	0.0	0.0001	300	0.0	1.94
detonation speed 7.782 km/s						
VN spike	0.32706	4.385	43.6	1586	2.96	8.13
CJ state	0.39808	1.833	28.2	2955	1.91	5.87
without energy release from slow reaction						
detonation speed 7.618 km/s						
VN spike	0.33124	4.029	41.0	1490	2.84	8.03
CJ state	0.40026	1.698	26.6	2510	1.84	5.78

2.1 SURF rate

The reaction progress variable for the SURF model (fast hot-spot reaction) is determined as a function of a dimensionless reaction-scale variable s and a reaction-scale function $g(s)$;

$$\lambda = g(s) , \quad (1a)$$

$$\frac{d}{dt}s = \tilde{f}(p_s, p) = f(p_s) \cdot \begin{cases} 0 , & \text{for } p \leq 0 \\ \left[\frac{p}{p_s}\right]^n , & \text{for } 0 < p < p_s \\ \left[\frac{p}{p_s}\right]^{n_{hi}} , & \text{for } p_s \leq p \end{cases} \quad (1b)$$

where $f(p_s)$ is a shock-strength function representing the number density of hot spots activated by the lead shock, n and n_{hi} are model parameters, and p_s is the shock pressure from the shock detector algorithm, see [Menikoff, 2016a]. In addition, $f(p_s)$ is taken to be zero unless a shock is detected or $p_s > p_{burn}$, where p_{burn} is a threshold pressure parameter to start burning introduced in [Menikoff, 2016a]. The parameter n_{hi} can help fit embedded velocity gauge data at late time for shock-to-detonation transition experiments. It has not been used for previous calibration and will not be used here; *i.e.*, $n_{hi} = 0$ corresponds to previous fitting form.

The fitting forms used for the reaction-scale function is taken to be

$$g(s) = 1 - \exp(-s^2) . \quad (2)$$

This can be associated with cylindrically expanding deflagration wavelets from randomly distributed hot spots. It gives a good fit to the profile shape of embedded velocity gauge data for shock-to-detonation transition experiments; see [Menikoff, 2015].

With pressure and time scales p_{scale} and t_{scale} , respectively, the fitting form for the shock-strength function is given by

$$f(p_s) = \begin{cases} 0 & \text{for } p_s \leq p_0, \\ c_{low} \left[\frac{p_s - p_0}{p_{\text{scale}}} \right]^{fn_{low}} & \text{for } p_0 < p_s \leq p_{low}, \\ c \left[\frac{p_s}{p_{\text{scale}}} \right]^{fn} & \text{for } p_{low} < p_s \leq p_1, \\ f(p_1) \cdot \exp \left[fn \cdot \ln(p_s/p_1) \cdot (1 - B_2 \ln(p_s/p_1)) \right] & \text{for } p_1 < p_s \leq p_{hi} \\ f_{max} & \text{for } p_{hi} < p_s . \end{cases} \quad (3)$$

With derived parameters

$$\begin{aligned}
fn_{low} &= [1 - p_0/p_{low}] f_n , \\
c_{low} &= c \cdot (p_{low}/p_{scale})^{f_n} \cdot \left[\frac{p_{scale}}{p_{low} - p_0} \right]^{fn_{low}} , \\
B_2 &= \frac{1}{2 \ln(p_{hi}/p_1)} , \\
f_{max} &= f(p_1) \exp\left[\frac{1}{2} f_n \ln(p_{hi}/p_1)\right] ,
\end{aligned}$$

f and f' are continuous at the end points of the pressure intervals; p_0 , p_{low} , p_1 , p_{hi} .

The high pressure region $p_s > p_1$ has been modified from what we previously used. The idea is that the hot-spot rate should saturate at a high pressure comparable to the von Neumann spike pressure of a CJ detonation. For a sufficiently overdriven detonation wave, the temperature behind the lead shock becomes large enough for the bulk chemical rate to exceed the hot-spot rate. This can be accounted for with the addition of an Arrhenius rate. We note that the high pressure modification has a negligible effect on parameters previously calibrated to shock initiation data.

The current form for $f(p_s)$ has 4 pressure transition points (p_0 , p_{low} , p_1 , p_{hi}) and 3 dimensionless parameters $C = c \cdot t_{scale}$, f_n and n . The number of parameters is the same as the previous fitting form [Menikoff \[2017a\]](#). The pressures p_0 , p_{low} , p_1 and parameters C , f_n can be fit to Pop plot data. The fit is not sensitive to p_1 provided that p_1 is greater than about $\frac{2}{3}p_{cj}$.

With SURFplus parameters from previous calibration [[Menikoff, 2017a](#), table 2] along with the best fit to Pop plot ($C = 2.8 \times 10^{-5}$ and $f_n = 4.25$) and a slight change of the parameter n from 3.0 to 3.2, simulations give a failure diameter between 8 and 10 mm. This is in fair agreement with the diameter effect data of [[Campbell, 1984](#), table 2]. However, the limiting detonation speed is 3.6% too low; 7.15 compared to 7.42 km/s. Correcting the EOS to get a higher CJ detonation speed helps, but still gives too low a value of the limiting detonation speed. This implies that the curvature effect is too large.

A smaller curvature effect (*i.e.*, smaller velocity deficit, $D_{cj} - D_n(\kappa)$) requires a smaller reaction-zone width, hence increasing the transition pressure p_1 and setting p_{hi} higher. A side effect is to increase the burn rate for pressures in the 15 to 18 GPa range critical for the failure diameter. This must be compensated for with a larger value of n , see Eq. (1b). A side effect of a larger value of n is to increase the reaction-zone width and hence the curvature effect. Thus the effect of the parameters are coupled. Iterating with the parameters p_1 , p_{hi} and n , a good fit to the failure diameter and limiting detonation speed are obtained with the SURFplus model parameters listed in table 2. Simulations results are shown in the next section.

The old and new burn rates are plotted in fig. 1. The slight difference between the rates for $p_s < 20$ GPa is mostly due to refitting shock initiation data (parameters C and f_n) due to the change in the products EOS. The large difference for $p_s > 25$ GPa is due to the larger value of n and the need for a smaller reaction-zone width. At the VN spike pressure, the rate is roughly a

Table 2: SURFplus parameters for PBX 9502. Functional form for the SURF rate is given in Eq. (1b) and Eq. (3). Parameter s_1 cuts off the exponential tail of $\lambda = g(s)$, see [Menikoff, 2016a, eq. (D.2)]. Carbon clustering parameters are defined in appendices B.1 and D.1 of [Menikoff, 2016a].

SURF parameters	
p_{scale}	1 GPa
t_{scale}	1 μ s
P_0	6.0
P_{low}	8.0
P_1	26
P_{hi}	55
C	3.4e-5
f_n	4.15
n	3.6
n_{hi}	0.0
s_1	2.0
P_{burn}	15.

Carbon clustering parameters

$Nratio$	250.0
Q	2.0
t_1	0.15
t_2	0.35
h_1	0.2
h_2	0.8

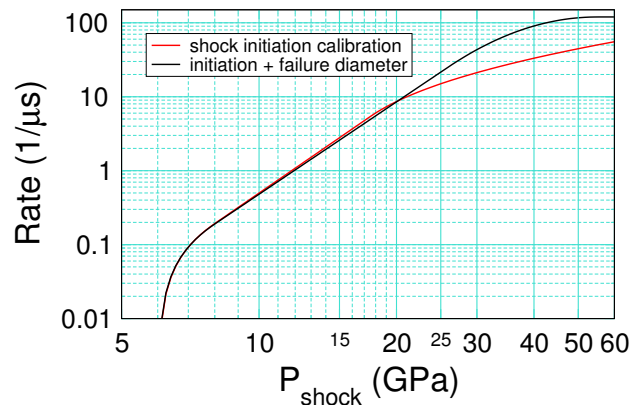


Figure 1: SURF rate for PBX 9502 $f(p_s)$, Eq. (3), for previous calibration to shock initiation data, and current calibration to both shock initiation and failure diameter.

factor of 3 greater. To get the full advantage of the smaller reaction-zone width on the curvature effect for the new rate requires finer zoning than needed for the old rate

We note that both the curvature effect [see [Hill and Aslam, 2010](#), fig. 6] and distance-of-run to detonation for shock initiation (Pop plot) [see [Gustavsen et al., 2006](#), fig. 10] depend to some extent on the PBX lot. Initiation appears less sensitive than the curvature effect partly because of the log-log scales used for the Pop plot. Moreover, the failure diameter is a threshold effect. The failure diameter depends on the burn rate in an intermediate pressure interval; between the upper end of shock initiation data and the lower end of detonation pressures for curved waves. The same intermediate pressure interval is also important for corner turning and the size of dead zones. How the lot dependence is related to the hot-spot distribution due to grain scale heterogeneities is an interesting question.

3 Numerics

Simulations discussed in the next section use the `xRage` code. `xRage` is an Eulerian adaptive mesh hydro code. The mesh can be refined locally by a factor of 2 per refinement level. The adaptive mesh capability is used to better resolve the narrow reaction zone of a propagating detonation wave.

The key input parameters that affect the grid resolution are as follows:

1. `dxset` = 0.5 mm
Level 1 (coarsest) grid cell size.
2. `sizemat`=0.015 mm
Refine down to this cell size (level 6 grid) to resolve gradients in 9502 reactants and products. This affects the slow carbon clustering reaction part of the reaction zone.
3. `he_zone_size`= 0.015 mm
Refines fast hot-spot reaction part of the reaction zone down to this cell size (level 6 grid).
4. `he_refine_dw`=0.001
Refines reacting region to next level only if $\frac{\Delta x}{D_{cj}} f(P_s) > dw$. This is intended to limit refinement in dead zones or slow burning regions for which the burning has a small effect on the flow. With fine resolution, a small change in the burn fraction per time step reduces truncation error from the operator split treatment of the reaction source terms.

At the above resolution, the 2-D simulations take up to 4 hours on 32 processors (Intel Xeon E5-2670 @ 2.6 GHz). This is long compared to the run time for a set of 5 1-D simulations used to evaluate the Pop plot metric for one parameter set in the calibration of the shock initiation parameters [Menikoff, 2017a], which is on average 20 minutes on 1 processor. Consequently, it is important to calibrate SURF rate model parameters sequentially starting with those for the pressure regime $p_s < p_1$ that dominates shock initiation.

3.1 Setup

The setup for failure diameter simulations is shown in fig. 2. The HE is initiated at the bottom and the detonation wave propagates up the cylinder. The configuration is similar to that used for the experiments of Lorenz et al. [2010]. Detonation wave in wide cylinder is used to initiate the

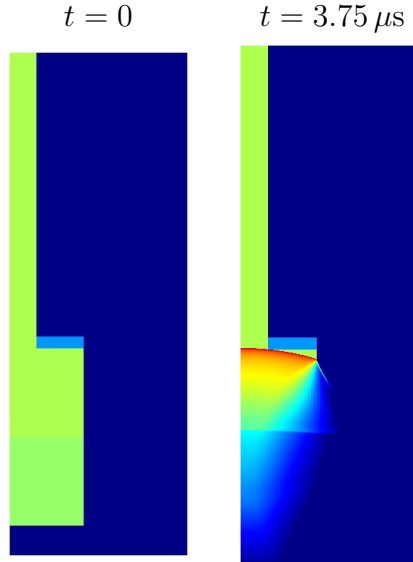


Figure 2: Density plots at setup and when detonation wave reaches start of narrow test cylinder. Domain is $0 < x < 30$ mm and $-20 < y < 65$ mm with cylindrical axis on left. At setup ($t = 0$), green is PBX 9502, and lighter shade of green is PBX 9501. Dark blue is air, and lighter shade of blue is PMMA collar. Radius of wide HE cylinder is 12.5 mm. Radius of test cylinder varies between 4 and 5 mm. Wide cylinders of 9501 and 9502 are each 15 mm long with y origin at the 9501/9502 interface. Test cylinder of 9502 is 50 mm long ($15 < y < 65$ mm). PMMA collar, 2 mm thick, is intended to block detonation products escaping from the wide cylinder. At $t = 3.75 \mu\text{s}$, detonation wave is propagating up, and the detonation front corresponds to the leading edge of the red region.

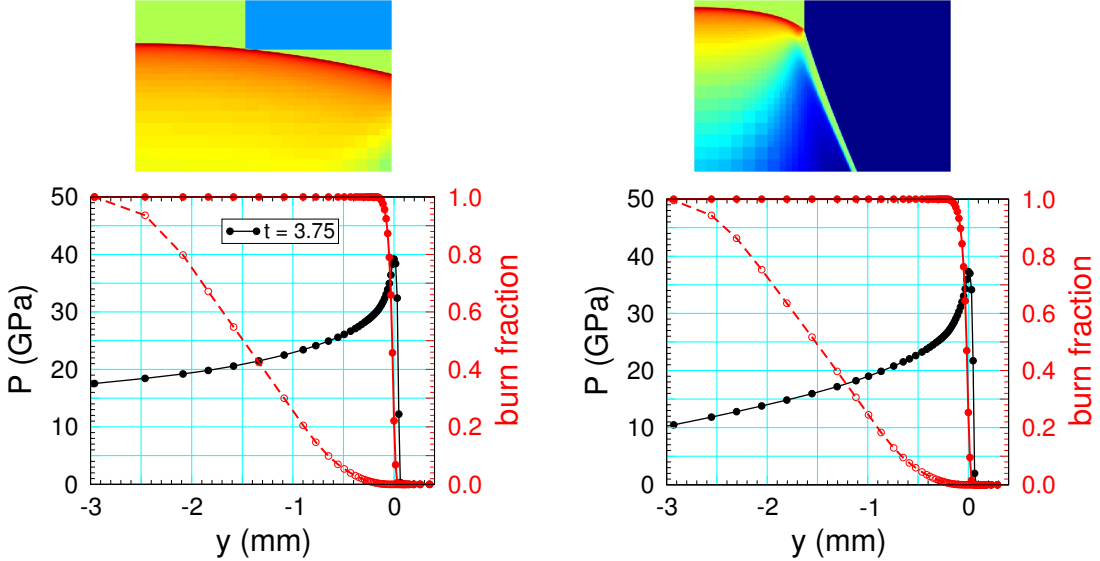


Figure 3: Density plots showing detonation front curvature, and pressure and reaction profiles on axis for simulation with test cylinder diameter just above the failure diameter. Left and right plots are when detonation front is at start and end of test cylinder, respectively. Solid and dashed red curves are fast hot-spot reaction and slow carbon clustering reaction progress variables, respectively. Symbols denote grid cells.

narrow test cylinder. The test cylinder length is greater than 5 times its diameter for simulation diameters of 10 mm or less. We note that the measured failure diameter is a little above 8 mm.

For simulation just above the failure diameter, the detonation front and profiles on axis when the detonation wave reaches the start and end of the test cylinder are shown in fig. 3. Compared to the steady detonation wave at the end of the test cylinder, the detonation at the start of the test cylinder has a slightly higher pressure and the front is less curved. Consequently, the test cylinder is slightly overdriven. Compared to initiation with a detonator and booster, as in the diameter effect experiments of [Campbell \[1984\]](#), less distance of run (*i.e.*, cylinder with lower length to diameter ratio) should be needed to determine whether or not a steady detonation wave can propagate in the test cylinder.

The profiles in fig. 3 also show the change in cell size due to the adaptive mesh. The fast hot-spot reaction occurs over 8 to 10 cells. The slow carbon clustering reaction is well resolved.

Next we show results of simulations that bound the failure diameter. At a radius of 4.5 mm the detonation wave propagates, while at 4.0 mm the detonation wave dies out.

3.2 Above failure diameter

For simulation with test cylinder radius of 4.5 mm, which is slightly above the failure diameter, the detonation wave propagates to the end of the cylinder.

Figure 4 shows that the detonation speed on axis. After a transient due to the initial overdrive, the detonation speed is nearly constant. Slight velocity fluctuations are due to when the numerical timing pins (probe points on axis 4.5 mm apart) trigger. Taking the difference over every other pin cuts down the magnitude of the fluctuations. The detonation speed of 7.4 km/s at a diameter of 9.0 mm is low compared to experimental value [Campbell, 1984, table 2] of 7.456 km/s by 0.75 %. This implies that the curvature effect and hence the reaction-zone width is slightly too large. Finer zoning would reduce the error slightly.

As a further check on whether the detonation is steady or decaying, Eulerian time histories of pressure are plotted in fig. 5 for a series of axial positions 1 radii apart at several radii. As expected the peak pressure decreases as the radius increases. But up to 4.5 diameters of run, there is no indication of decay.

2-D plots when the detonation wave is near the end of the test cylinder are shown in fig. 6. The pressure plot shows a rarefaction behind the detonation front at the HE/air interface. Combined with the factor $(P/P_s)^n$ in the burn rate, Eq. (1b), this leads to a partially burned HE boundary layer seen in the volume fraction plot. The incomplete burn also results in a lower temperature and hence higher HE density adjacent to the air interface seen in the density plot. The advected shock pressure plot shows that the lead shock is steady and provides another check that the detonation wave is not decaying.

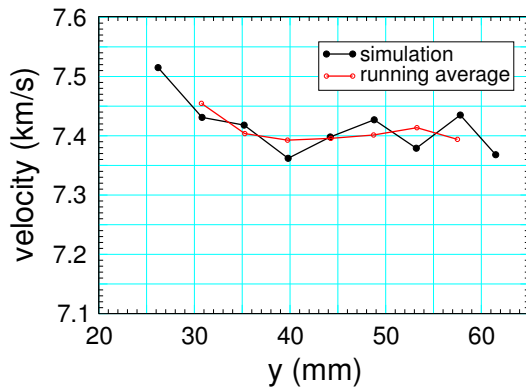


Figure 4: Detonation velocity, from numerical timing pins on axis, in test cylinder, $15 < y < 65$ mm. Running average is over 3 points.

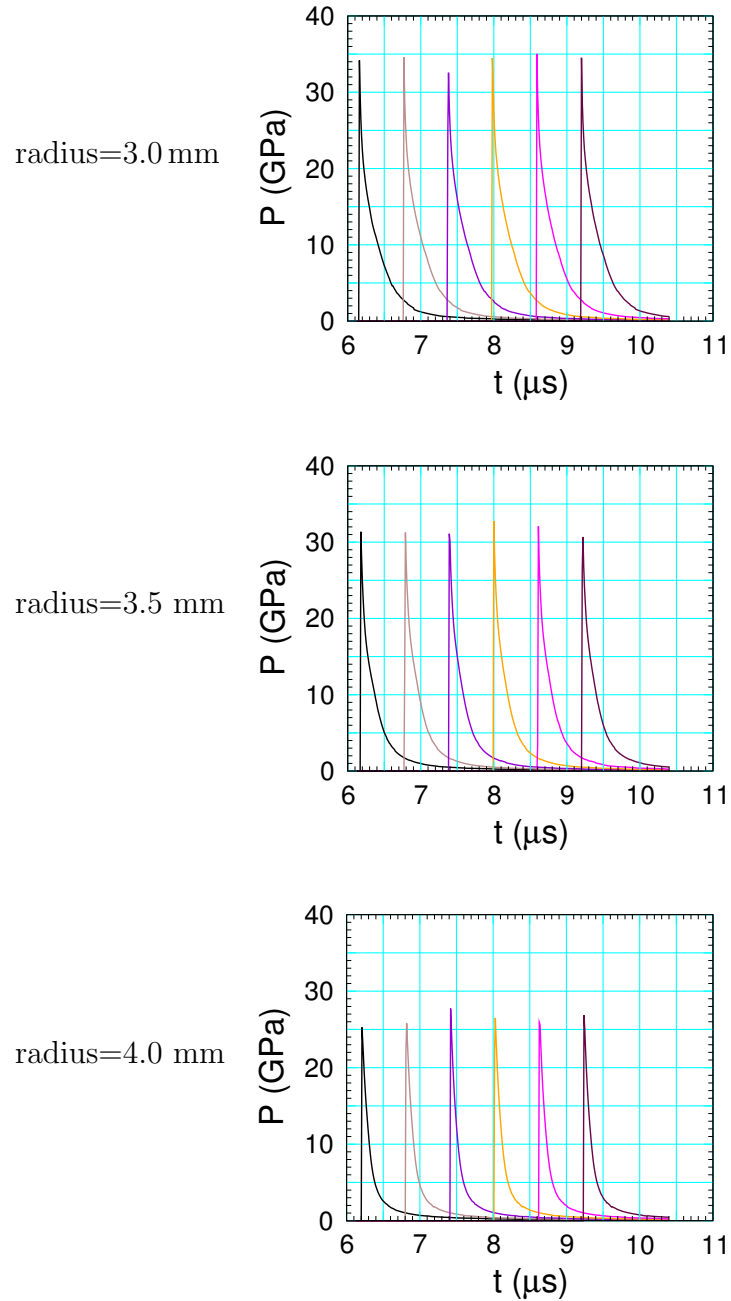


Figure 5: Pressure time histories at fixed radius and increasing distances of run; $y = 18, 22.5, 27, 31.5, 36, 40.5$ mm, relative to the start of the test cylinder.

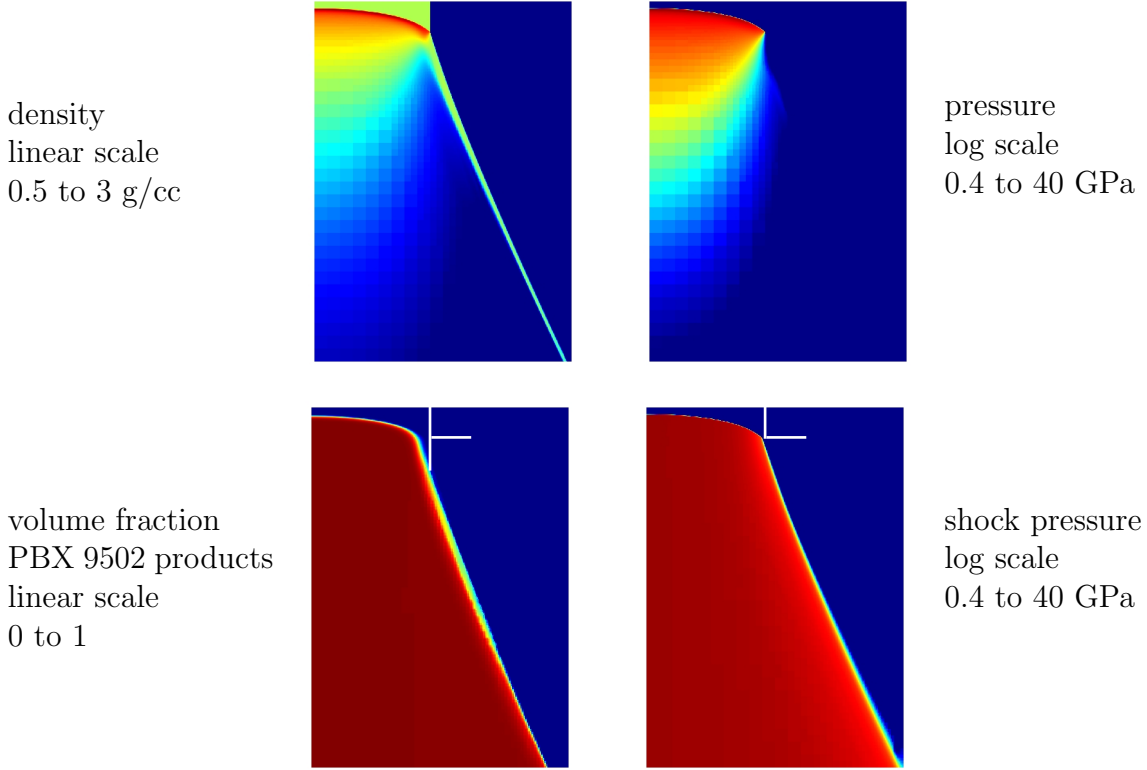


Figure 6: 2-D variable plots at end of simulation ($t = 10.4 \mu\text{s}$). Plot domain $0 < x < 10 \text{ mm}$, $51 < y < 65 \text{ mm}$. Color scale blue to red is from low to high. The vertical and horizontal white lines on the bottom plots denote the initial PBX9502 boundary and y-position of the shock, respectively. For the SURFplus model, the products volume fraction of 1 corresponds to the completion of the fast hot-spot reaction. The completion of the carbon clustering energy release occurs further behind the detonation front.

It is instructive to examine pressure and reaction profiles at different radii shown in fig. 7. Several points to note:

1. As expected the peak pressure decrease with increasing radius due to the curvature of the detonation front.
2. Almost all the slow reaction, even on the axis, occurs in the supersonic region with respect to the detonation front; *i.e.*, $D > u + c$. Hence, the energy release from carbon clustering does not contribute to driving the detonation wave.
3. The subsonic region behind the lead shock ($D < u + c$) decreases in axial extent with increasing radius. Moreover, the state behind the lead shock appears to be approaching

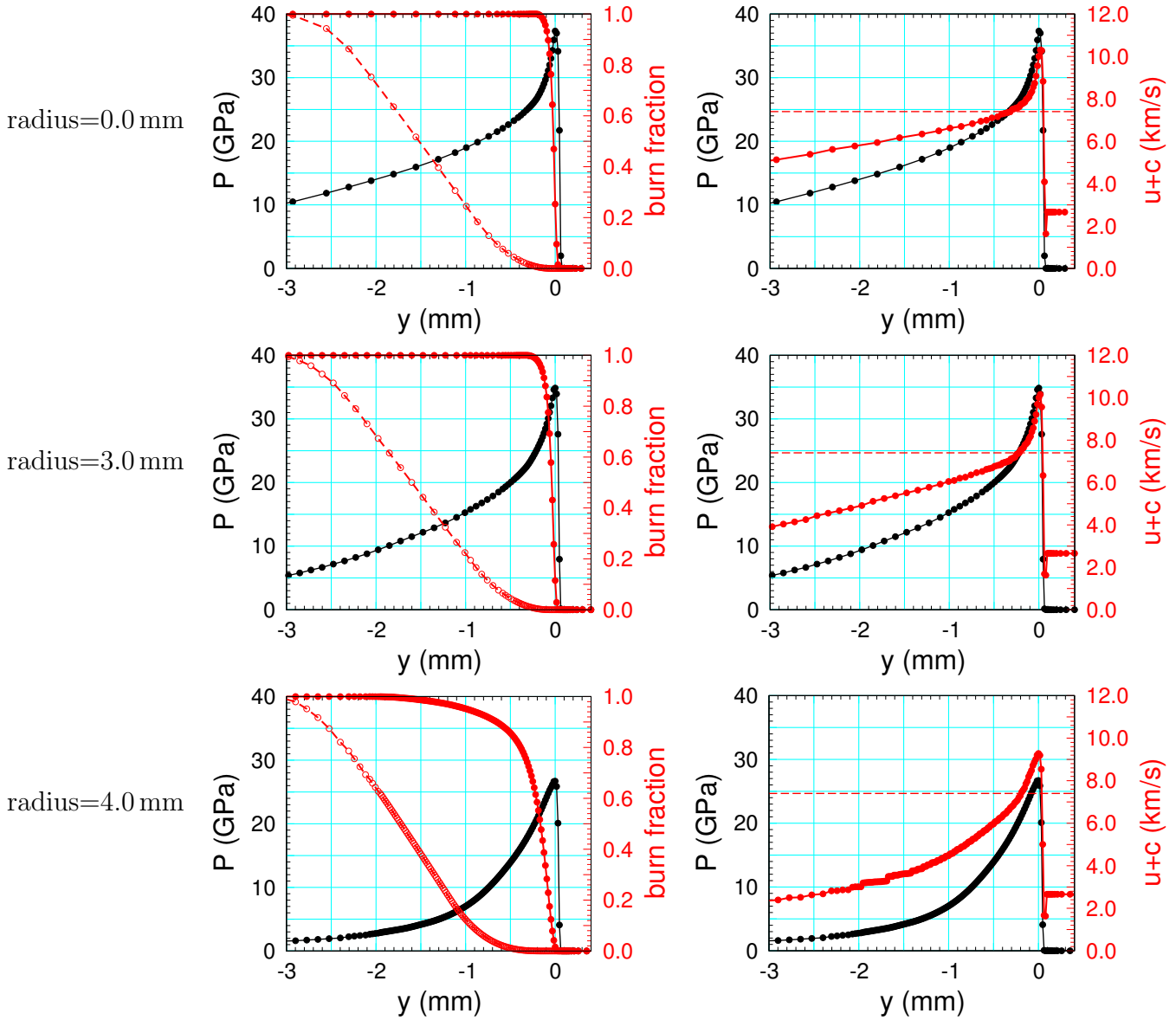


Figure 7: Profile plots at end of simulation ($t = 10.4\mu\text{s}$). Left plots show pressure and reaction progress variables; solid and dashed red curves are the fast hot-spot reaction and the slow carbon clustering reaction, respectively. Right plots show pressure, characteristic speed ($u + c$) and detonation speed (dashed red line) from fig. 4. The spatial origin has been shifted to the wave front. (Continued on next page.)

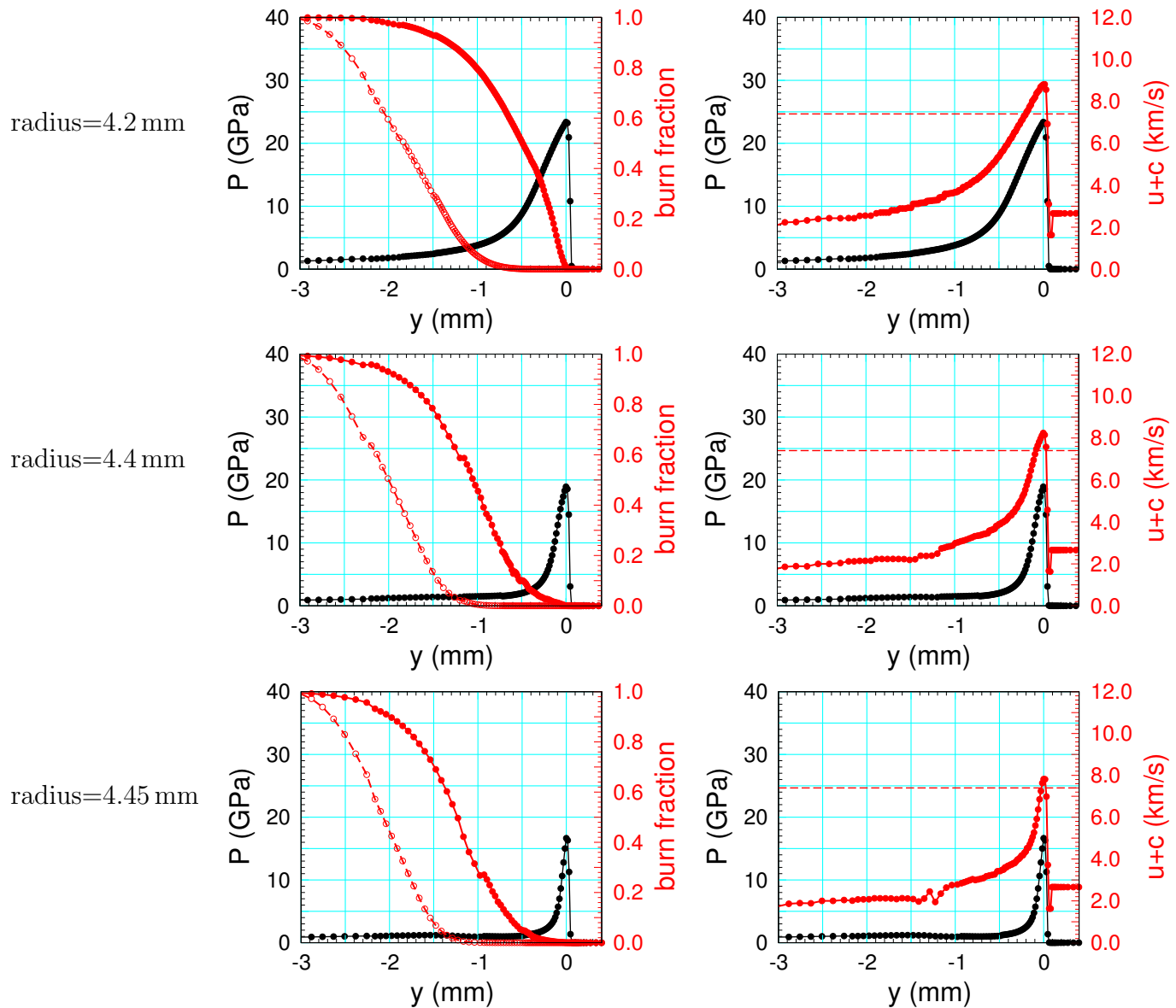


Figure 7 (continued): Profiles near HE boundary.

the sonic condition at the HE boundary. This boundary feature has been conjectured based on the analysis of [Trofimov and Dremin, 1971, see fig. 1c] and [Bdzil, 1981, see fig. 14], and seen in numerical simulations of [Gamezo and Oran, 1997, see fig. 1]. For the reactants 9502 EOS, the sonic point on the shock polar (with the ahead velocity as the detonation speed) has a shock pressure of 14.4 GPa and shock speed of 5.44 km/s. We note that the sonic pressure is within the upper end of the measured Pop plot data. Consequently, the burn rate at the sonic pressure is determined by shock initiation data. From fig. 1 the rate at the sonic pressure is over an order of magnitude smaller than the rate at the VN spike pressure of a planar detonation wave.

4. Near the HE boundary (radius greater than about 4 mm) there is not enough reaction within the subsonic region to drive a detonation wave. Instead the lead shock is driven by the high pressure from the detonation wave in the interior of the HE (*i.e.*, at lower radii). The lead shock does generate hot spots which leads to a low reaction rate and a long reaction region near the HE/air interface as seen in products volume fraction plot of fig. 6.

Items 3 and 4 above have implications for DSD theory; see [Bdzil and Stewart, 2007] and references therein. Namely, the detonation speed as a function of front curvature, $D_n(\kappa)$, based on a quasi-steady 1-D reaction-zone profile with a given front curvature (in context of SURFplus model see [Menikoff and Shaw, 2012]) does not extend to large enough κ (*i.e.*, with low enough detonation pressure) to correspond to the boundary pressure of an unconfined rate stick. We note that the reaction zone of a quasi-steady 1-D detonation wave corresponds to a profile along a streamline in the rest frame of the detonation front. Since the streamline moves radial outward, the pressure would fall off faster and the products burn fraction grow slower than in the profile plots at constant radius shown in fig. 7.

This claim is supported by measurements of $D_n(\kappa)$ using rate sticks of different diameters (10, 18, 50 mm). Starting at $\kappa > 0.2 \text{ mm}^{-1}$, the $D_n(\kappa)$ curves start to diverge; see [Hill et al., 1998, fig. 6]. Moreover, the difference increases as κ increases. Furthermore, the measured front curvature has a qualitative change in behavior with κ varying very rapidly near the HE/air interface [Hill et al., 1998, see figs. 3 and 4]. That is, the large κ values that give low D_n correspond to a very small portion of the front near the boundary (*e.g.*, on a 25 mm radius rate stick $\kappa > 0.5 \text{ mm}^{-1}$ occurs only for radii within to 0.3 mm of the interface). This is important for DSD theory since the boundary condition at the interface affects the shape of the detonation front in the interior of the HE and hence the diameter effect inferred from the curvature effect.

The shape of the detonation front and the lead shock pressure at the end of the simulation are shown in fig. 8. The plot shows the rapid fall off in the shock pressure in the neighborhood

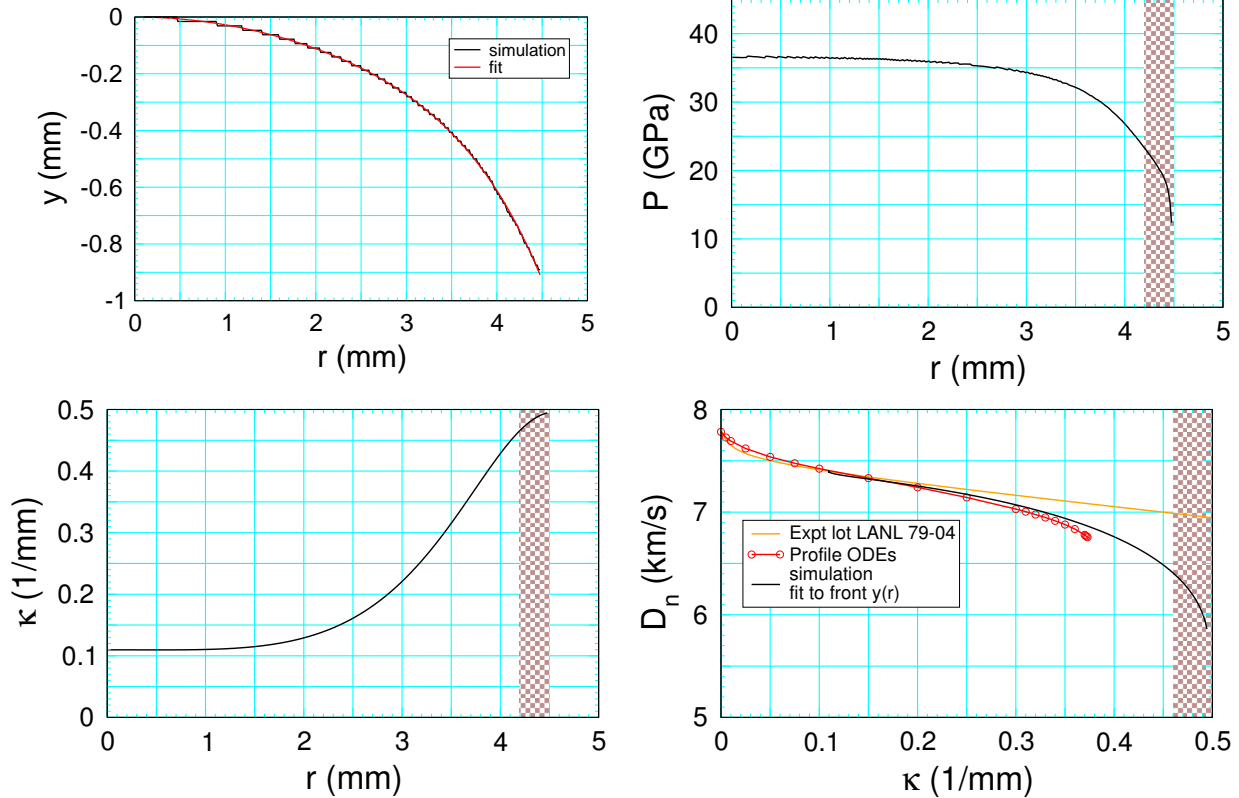


Figure 8: Detonation front plots at the end of simulation ($t = 10.4 \mu\text{s}$); front shape $y(r)$, lead shock pressure $P_s(r)$, front curvature $\kappa(r)$ and detonation speed normal to the front $D_n(\kappa)$. Stairstep in curve of $y(r)$ is due to the cell size of 0.015 mm. $\kappa(r)$ and $D_n(\kappa)$ are computed from fit to $y(r)$. Shaded brown region corresponds to portion of front with shock pressure too low to support a quasi-steady detonation wave profile. On the $D_n(\kappa)$ plot, two additional curves are shown. The first is from the fit to curvature data [Hill and Aslam, 2010] for same lot (LANL 79-04) as used by Campbell [1984] for the diameter effect experiments. The second is from the quasi-steady detonation profile ODEs [Menikoff and Shaw, 2012] using the same SURFplus model parameters as the 2-D simulation.

of the HE interface. Based on the axial detonation speed and the shape of the front $y(r)$, the detonation speed normal to the front D_n and the front curvature κ can be computed in a similar manner as is done for the experimental determination; see [Hill et al., 1998, Eqs. 1-4]. Plots of $\kappa(r)$ and $D_n(\kappa)$ are also shown in fig. 8.

A fit is used to smooth $y(r)$ in order to take the first and second derivatives needed to compute the curvature and the normal detonation speed. We use the same fitting form as in [Hill et al., 1998, Eq. 1]. Even imposing the constraint that κ is monotonic, there is some

uncertainty in computing κ and to a lesser extent D_n due to the number of terms used in the fit, the fitting parameter η , and the numerical resolution from the cell size and the rarefaction from the shock interaction at the HE/air interface. The uncertainty is largest in the last few tenths of mm adjacent to the interface, partly because the ‘global’ fitting form does not capture the change in behavior near the HE boundary. The shaded brown region of fig. 8 is based on fig. 7 and corresponds to the portion of the front in which the reaction occurs too far behind the sonic point to support the lead shock.

The plot of $D_n(\kappa)$ also shows curves from fits to experimental curvature effect data [Hill and Aslam, 2010, table 1 and Eqs. 2-5] using the same lot (LANL 79-04) as used in the diameter effect experiments of Campbell [1984] we are using for the failure diameter, and from the quasi-steady detonation wave profile ODEs [see Menikoff and Shaw, 2012]. We note two points:

1. $D_n(\kappa)$ from the 2-D simulation and the ODEs are consistent up to $\kappa = 0.37 \text{ mm}^{-1}$. For larger κ , the burn model does not have a quasi-steady detonation wave profile. The detonation wave profile in the simulation with larger curvatures is likely due to transverse flow within the reaction zone. The non-existence of detonation profiles near the boundary implies the conjecture that the failure diameter is determined from the extinction point on the $D_n(\kappa)$ curve [see, Stewart and Yao, 1998] is not true.
2. $D_n(\kappa)$ from the 2-D simulation and the fit to curvature effect data are consistent up to $\kappa = 0.2 \text{ mm}^{-1}$. For larger κ , the simulation gives a lower D_n . Again this is likely due to transverse flow within the reaction zone.

A key question is whether the difference of $D_n(\kappa)$ between the simulation and the curvature effect data fit is due to the choice of reactive burn model or the interpretation of the curvature effect data. We conjecture it is due to the sonic point at the HE/air interface which does not allow for a reactive wave profile in the neighborhood of the HE boundary.

3.3 Below failure diameter

For simulation with test cylinder radius of 4.0 mm, which is slightly below the failure diameter, a detonation wave is initiated by the overdrive shown in fig. 2 but fails to propagate to the end of the cylinder. The detonation speed on axis, shown in fig. 9, slowly decreases and then stops abruptly at $y = 41 \text{ mm}$ (26 mm from start of test cylinder) when the lead shock pressure drops below the numerical threshold (10 GPa) for the timing pins from which the speed is derived.

Plots of the shock pressure and volume fraction are shown in fig. 10. We note that the shock pressure and volume fraction variables are advected with the flow. The finger on the right side

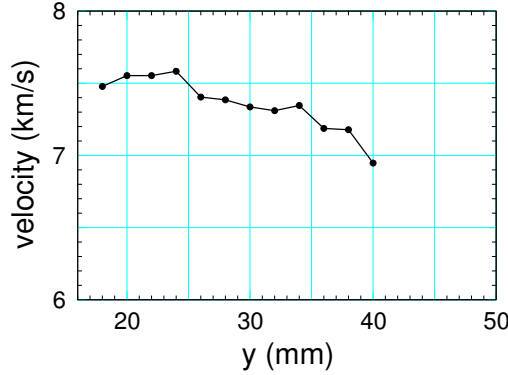


Figure 9: Detonation speed on axis in test cylinder, $15 < y < 50$ mm.

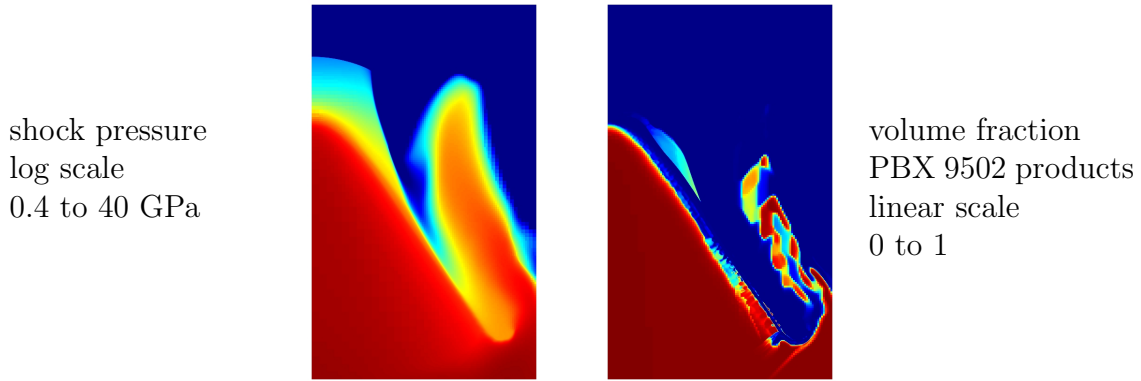


Figure 10: 2-D plots at $t = 8.75 \mu\text{s}$ of shock pressure and products volume fraction. Plot domain $0 < x < 15$ mm, $25 < y < 50$ mm. Color scale blue to red is from low to high. For the SURFplus model, the products volume fraction of 1 corresponds to the completion of the fast hot-spot reaction. The completion of the carbon clustering energy release occurs further behind the detonation front.

of the plots is due to advection of partly burned 9502 from the wide diameter cylinder past the PMMA collar, see fig. 2. It does not affect the flow in the test cylinder. Ignoring the finger, both plots show that the detonation wave fails starting at the HE boundary and propagating radial inward to the axis. After the detonation wave fails, a weak shock continues to propagate up the test cylinder.

More details of how the detonation wave fails are shown in plots of Eulerian time histories for a series of axial positions at different radii. In fig. 11 it is seen that at smaller radii the pressure fall off starts at a later time and then follows a similar progression as occurred earlier at larger radii. Again this implies that the failure of the detonation progresses from the boundary radially inward to the axis.

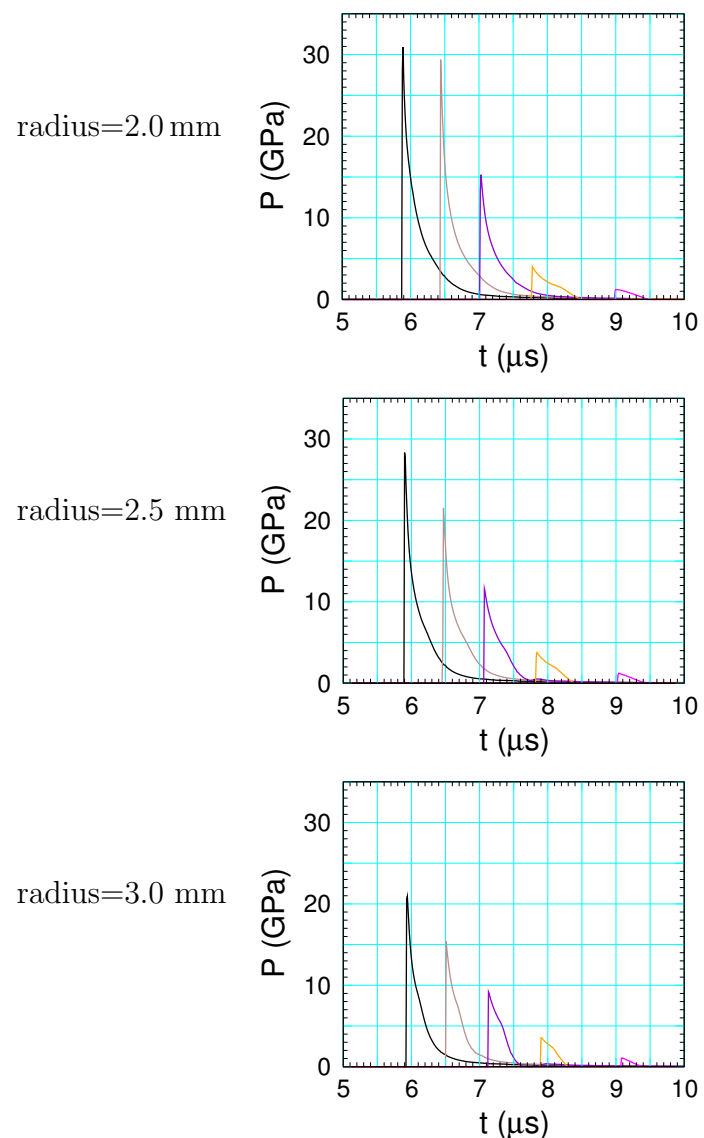


Figure 11: Pressure time history at fixed radius and increasing distances of run; $y = 16, 20, 24, 28, 32$ mm, relative to the start of the narrow HE cylinder.

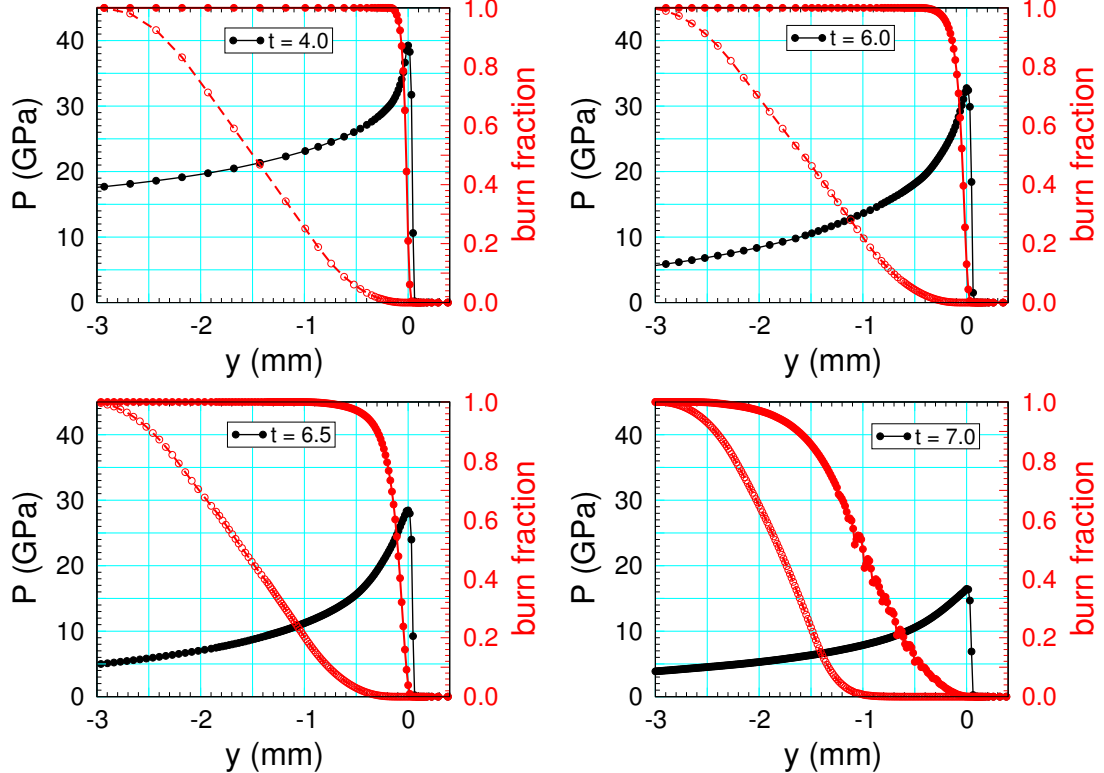


Figure 12: Profiles of pressure and reaction progress variables at a radius of 2 mm and selected sequence of times. The solid and dashed red curves are the fast hot-spot reaction and the slow carbon clustering reaction, respectively. The spatial origin has been shifted to the lead shock front.

The evolution of pressure and reaction variable profiles at half radius (2 mm) are shown in fig. 12. As time increases, the lead shock pressure decreases. This decreases the burn rate and results in the bulk of the hot-spot reaction occurring further and further behind the lead shock. The decrease in the shock pressure and the burn rate also results in a smaller pressure gradient behind the lead shock. This lowers the further decay rate of the lead shock decays.

2-D plots when the detonation front extends about a third of the test cylinder radius are shown in fig. 13. The lower shock pressure can be seen progressing inwards and causing the detonation wave to decay and failure occurring over the outer 2/3 radii of the front. It is noteworthy that the failure of the detonation wave evolves in a continuous manner. There is no discontinuity in the lead shock pressure or kink in the shock front, and no rarefaction wave emanating from the shock front other than the expected one at the HE/air interface. The failure of the detonation wave is evident in the evolution of the smeared out contact between the HE products and reactants that forms behind the lead shock.

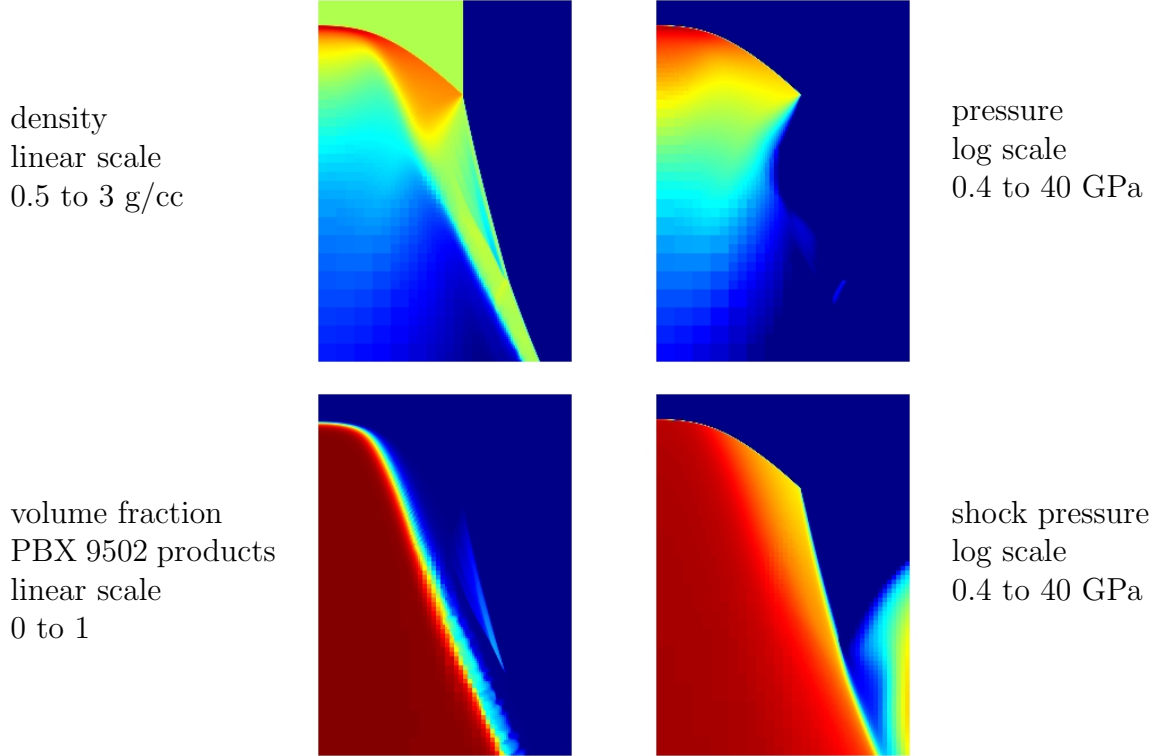


Figure 13: 2-D variable plots at $t = 7 \mu\text{s}$. Plot domain $0 < x < 7 \text{ mm}$, $30 < y < 40 \text{ mm}$. Color scale blue to red is from low to high. For the SURFplus model, the products volume fraction of 1 corresponds to the completion of the fast hot-spot reaction. The completion of the carbon clustering energy release occurs further behind the detonation front.

3.3.1 Failure mechanism

Based on the plots and observations of the simulation in which the detonation wave decays, the failure mechanism can be explained in terms of two effects. First, there is a variation of the lead shock pressure due to the front curvature. The transverse pressure gradient is largest at the HE/air interface where a steady detonation would have a low pressure corresponding to the sonic condition on the reactants shock polar. This will cause a transverse flow within the reaction zone towards greater radii. Second, evolution of the lead shock strength is determined by the shock change equation for the Riemann invariant at the shock front, see [Menikoff, 2016b, Eq. 2]

$$(\mathbf{d}/dt) \mathbf{R}_s^+ = -(u + c - D) \partial_y \mathbf{R}^+ + (\partial_\lambda P)_{V,e} (\mathbf{d}/dt) \lambda - \rho c^2 u \kappa , \quad (4)$$

where on the right hand side the first term is related to the pressure derivative along the streamline in the rest frame of the wave front (y direction), the second term is from the burn rate, and the third term is due to the geometric divergence from the front curvature. The shock strength, as measured by the shock pressure, will increase (or decrease) if $(d/dt) R_s^+$ is positive (or negative). For a steady wave, $(d/dt) R_s^+ = 0$ and there must be a balance between the rate term and the pressure derivative term plus the divergence term.

The transverse flow can change the pressure derivative which affects the lead shock speed and front curvature. If the rate, which depends on the lead shock strength, decreases faster than the front curvature and reaction-zone profile can adjust to compensate then the right hand side of Eq. (4) becomes sufficiently negative for the shock pressure to continue to decrease. This increases the transverse pressure gradient and hence the transverse flow. The shock change source terms for the transverse-upstream reaction zone can then get out of balance. If the effect propagates transversely inward, then the detonation wave will fail.

4 Summary

The failure diameter and the limiting detonation speed just above the failure diameter can be used to set SURF rate parameters for shock pressures above the range that is important for shock initiation with a sustained shock; *i.e.*, above the measured Pop plot data. We note that the critical pressure for the failure diameter is the sonic pressure on the reactants shock polar. This is comparable to the shock pressure at the high end of Pop plot data. For PBX 9502, both pressures are about 15 GPa.

The relevant burn parameters for the failure diameter are the transition pressures p_1 and p_{hi} in Eq. (3) and n in Eq. (1b). For fixed transition pressures, increasing n will decrease the failure diameter. However, the limiting detonation speed depends on the curvature effect. This is affected by the burn rate above the CJ pressure and hence the need to adjust parameters p_1 and p_{hi} . We note that both the previous calibration in [Menikoff, 2017a] and parameters given here in table 2 fit both the Pop plot and failure diameter. They differ in the limiting detonation speed and the curvature effect, $D_n(\kappa)$. In addition, the 9502 products EOS used here was adjusted from that used in the previous calibration to increase the CJ detonation speed by about 1% [Menikoff, 2017b] in order to agree with the value derived from the diameter effect data of [Campbell, 1984].

Simulation results just above the failure diameter show three important features. First is the shock at the HE/air interface is sonic. This is in agreement with previous analysis. Second is that in the neighborhood of the HE/air interface the reaction along a streamline does not

support the lead shock; *i.e.*, the profile along a streamline does not correspond to quasi-steady 1-D detonation as assumed by DSD theory. Rather the shock in the neighborhood of the interface is supported by the detonation pressure in the interior of the HE. Third is the failure diameter is determined by the fast hot-spot rate. The slow energy release from the carbon clustering reaction occurs behind the sonic locus and does not contribute to determining either the front curvature or the detonation speed.

Below the failure diameter, the simulation results show that the failure of the detonation wave evolves in a continuous manner. The radial extent of the detonation front decreases until it reaches the axis and the detonation ceases to exist. This is the expected result that failure propagates inward from the HE boundary.

Two other detonation wave properties depend on the same burn rate parameters that dominate the failure diameter. The first is corner turning. When a detonation wave turns a corner, the lead shock pressure drops in the diffraction region. Similar issues with transverse flow along the lead front occur when the shock pressure is around the boundary pressure at the failure diameter. Second is shock initiation when there is a pressure decreasing gradient behind the lead shock. The rate parameter n affects the competition between reaction and pressure gradient in determining whether the lead shock strength increases, as is necessary for a shock-to-detonation transition.

We note that the reaction-zone width of the fast hot-spot reaction is important for the failure diameter and the curvature effect at moderate to large front curvature. With the resolution used here (0.015 mm cell size) there are only 8 cells in the fast reaction zone. Additional simulations varying the reaction zone refinement show small quantitative differences. With 4 times coarser cell size of 0.060 mm the failure diameter increase slightly (from between 8 and 9 mm to 9 and 10 mm), and with 4 times finer cell size of 0.004 mm the limiting detonation speed just above the failure diameter increases slightly (from 7.40 km/s to 7.42 km/s). There are also small differences in the front shape which affect the front curvature in the neighborhood of the HE/air interface.

Finally, it is important to note that data for the Pop plot, failure diameter and limiting detonation speed used to calibrate the SURFplus model depends on the initial density and initial temperature of the PBX and on the PBX lot. Consequently, the calibration determined here is for PBX 9502 at room temperature with initial density of 1.894 g/cc and the lot (LANL 79-04) used in the diameter effect experiments of [Campbell \[1984\]](#).

References

J. B. Bdzip. Steady-state two-dimensional detonation. *J. Fluid Mech.*, 108:195–226, 1981. [3](#), [16](#)

J. B. Bdzip and D. S. Stewart. The dynamics of detonation in explosive systems. *Annual Rev. Fluid Mech.*, 39:263–292, 2007. [2](#), [16](#)

A. W. Campbell. Diameter effect and failure diameter of a TATB based explosive. *Propellants, Explosives, Pyrotechnics*, 9:183–187, 1984. [2](#), [3](#), [4](#), [6](#), [10](#), [11](#), [17](#), [18](#), [23](#), [24](#)

A. W. Campbell and R. Engelke. The diameter effect in high-density heterogeneous explosives. In *Proceeding of the Sixth International Symposium on Detonation*, pages 642–652, 1976. [4](#)

V. N. Gamezo and E. S. Oran. Reaction-zone structure of a steady-state detonation wave in a cylindrical charge. *Combustion and Flame*, 109:253–265, 1997. [3](#), [16](#)

R. L. Gustavsen, S. A. Sheffield, and R. R. Alcon. Measurements of shock initiation in the tri-amino-tri-nitro-benzene based explosive PBX 9502: Wave forms from embedded gauges and comparison of four different material lots. *J. Appl. Phys.*, 99:114907, 2006. URL <http://dx.doi.org/10.1063/1.2195191>. [8](#)

L. G. Hill and T. D. Aslam. Detonation shock dynamics calibration for PBX 9502 with temperature, density and material lot variation. In *Proceeding of the Fourteenth International Symposium on Detonation*, pages 779–788, 2010. [2](#), [8](#), [17](#), [18](#)

L. G. Hill, J. B. Bdzip, and T. D. Aslam. Front curvature rate stick measurements and detonation shock dynamics calibration for PBX 9502 over a wide temperature range. In *Proceeding of the Eleventh International Symposium on Detonation*, pages 1029–1037, 1998. [16](#), [17](#)

K. T. Lorenz, D. E. Hare, P. Vitello, P. C. Souers, R. Chambers, and E. L. Lee. Detonation failure in small cylindrical LX-17 charges. In *Proceeding of the Fourteenth International Symposium on Detonation*, pages 1219–1228, 2010. [9](#)

R. Menikoff. Shock-to-detonation transition simulations. Technical Report LA-UR-15-25266, Los Alamos National Lab., 2015. URL <http://www.osti.gov/scitech/servlets/purl/1193613/>. [5](#)

R. Menikoff. Shock detector for SURF model. Technical Report LA-UR-16-20116, Los Alamos National Lab., 2016a. URL <http://www.osti.gov/scitech/servlets/purl/1234496>. [5](#), [7](#)

R. Menikoff. Barrier experiments: Shock initiation under complex loading. Technical Report LA-UR-16-20140, Los Alamos National Lab., 2016b. URL <https://www.osti.gov/scitech/servlets/purl/1234498>. 22

R. Menikoff. SURFplus model calibration strategy. Technical Report LA-UR-17-22073, Los Alamos National Lab., 2017a. URL <https://www.osti.gov/scitech/servlets/purl/1346849>. 2, 3, 6, 9, 23

R. Menikoff. Fine tuning the CJ detonation speed of a high explosive products equation of state. Technical Report LA-UR-17-23912, Los Alamos National Lab., 2017b. URL <https://www.osti.gov/scitech/servlets/purl/1357103>. 4, 23

R. Menikoff and M. S. Shaw. Reactive burn models and Ignition & Growth concept. *EPJ Web of Conferences*, 10, 2010. doi: 10.1051/epjconf/20101000003. URL http://www.epj-conferences.org/articles/epjconf/pdf/2010/09/epjconf_nmh2010_00003.pdf. 2

R. Menikoff and M. S. Shaw. The SURF model and the curvature effect for PBX 9502. *Combustion Theory And Modelling*, pages 1140–1169, 2012. URL <http://dx.doi.org/10.1080/13647830.2012.713994>. 2, 16, 17, 18

D. S. Stewart and J. Yao. The normal detonation shock velocity-curvature relation for materials with non-ideal equations of state and multiple turning points. *Combustion and Flame*, 113: 224–235, 1998. 18

V. S. Trofimov and A. N. Dremin. Structure of the nonideal detonation front in solid explosives. *Combustion, Explosion and Shock Waves*, 7:368–369, 1971. 3, 16